

# A Liquid-Metal Electrocatalyst as a Self-Healing Anchor to Suppress Polysulfide Shuttling in Lithium-Sulfur Batteries

Saisaban Fahad,<sup>[a]</sup> Zeyang Zhang,<sup>[a, c, d]</sup> Lei Zhai,<sup>[a, c, d]</sup> and Akihiro Kushima<sup>\*[a, b, c]</sup>

Lithium-sulfur battery (LSB) is a promising next generation energy storage technology due to its high theoretical capacity, low cost, and environmental friendliness surpassing current lithium-ion batteries. However, several challenges restrict the practical applications of LSBs. A major obstacle that limits its performance is the dissolution of long-chain lithium polysulfides into the electrolyte which results in loss of active material and capacity fade during the charge/discharge cycles. Here, we developed a novel sulfur composite with liquid-metal (LM) nanoparticles and reduced graphene oxide (rGO) dispensed on a carbon-cloth electrode to achieve long cycling of LSBs. The liquid nature of the LM nanoparticles results in many advan-

tages. It provides a strong anchoring with sulfur inhibiting the polysulfide shuttle effect. In addition, it prevents the detachment of the sulfur particles from the current collector albeit large volume changes and cracking of the sulfur during lithiation and delithiation, maintaining the electron conduction paths. This innovative composite resulted in a high discharge capacity, an outstanding capacity retention, and a high Coulombic efficiency. Our results demonstrate an effective method to suppress the polysulfide shuttle effect and pave a new path towards practical applications of LSBs by using multifunctional LM nanoparticles composites.

## Introduction

There are increasing demands for high energy density batteries with long cycle life and low cost for use in technology such as electric vehicles, electronic devices, and grid energy storages. Although lithium-ion battery (LIB) is a leading technology in the rechargeable battery field, development of next generation energy storage devices is anticipated to meet the requirements for the increasing energy storage demands.<sup>[1–4]</sup> Here, lithium-sulfur batteries (LSBs) are considered one of the promising candidates to meet the market demands due to their high theoretical capacity (1675 mAh g<sup>-1</sup>), high energy density (2600 Wh kg<sup>-1</sup>), inexpensive cost, nontoxicity, and the abundant availability of sulfur.<sup>[5–7]</sup> However, LSBs are not currently implemented in general applications. This is due to the insulating nature of sulfur and lithium sulfides, volume expansion during cycling which leads to structural changes of the electrode of up to 80% upon lithiation, and most

importantly, the dissolution of lithium polysulfides into the electrolyte during cycling leads to capacity decay and low Coulombic efficiency. Additionally, these lithium polysulfides can diffuse to the lithium anode and cause parasitic reactions at the anode (shuttle effect).<sup>[8–10]</sup>

Over the last decade, there has been a considerable amount of research conducted on LSBs to overcome these issues. Carbon materials with sulfur confining pores are frequently adopted for improving cycling performance due to their high electrical conductivity and large surface area.<sup>[11]</sup> Examples include carbon nanotubes,<sup>[12]</sup> porous carbon,<sup>[13]</sup> graphene oxide,<sup>[14]</sup> and carbon spheres.<sup>[15]</sup> However, the low binding energy between the non-polar carbon and polar lithium sulfide results in the incomplete trapping of the polysulfides.<sup>[16,17]</sup>

In addition, polar materials such as metal oxides, metal carbides and metal sulfides have proven effective in trapping polysulfides and providing more reaction sites.<sup>[17–19]</sup> Other modifications were achieved by using solid electrolytes,<sup>[20]</sup> selecting adequate binders,<sup>[21]</sup> employing lithium polysulfide catholyte,<sup>[22]</sup> inserting an interlayer,<sup>[23]</sup> and modifying separators.<sup>[24,25]</sup> Despite the improvements that have been achieved by these approaches, some procedures require complicated fabrication processes.

The use of reduced graphene oxide in the cathode composite is reported to improve the capacity and the cycle lifetime of LSBs due to its ability to trap lithium polysulfide preventing the shuttle effect.<sup>[26,27]</sup> Recently, the use of sulfur/gallium (S/Ga) hybrid material, such as S/Ga core-shell electrode,<sup>[28,29]</sup> 3D porous S/Ga composite cathode,<sup>[30]</sup> and gallium oxide shield layer on the separator,<sup>[31]</sup> were proposed to show exceptional electrochemical performances. Here, the gallium acted as an electrocatalyst by providing abundant adsorption and reaction sites for lithium polysulfides. These

[a] S. Fahad, Z. Zhang, Prof. L. Zhai, Prof. A. Kushima  
Department of Materials Science and Engineering  
University of Central Florida  
Orlando, FL 32816  
E-mail: kushima@ucf.edu

[b] Prof. A. Kushima  
Advanced Materials Processing and Analysis Center,  
University of Central Florida  
Orlando, FL 32816

[c] Z. Zhang, Prof. L. Zhai, Prof. A. Kushima  
NanoScience Technology Center  
University of Central Florida  
Orlando, Florida 32826, United States

[d] Z. Zhang, Prof. L. Zhai  
Department of Chemistry  
University of Central Florida  
Orlando, Florida 32816, United States

 Supporting information for this article is available on the WWW under  
<https://doi.org/10.1002/batt.202100395>

indicate the addition of both rGO and LM may play an important role in improving the cycling life of LSBs. Although Ga is a low melting point metal with melting temperature  $T_m$  of  $\sim 30^\circ\text{C}$ , it is a solid at operating temperatures of LSBs. By adding other alloying elements, Ga can further reduce  $T_m$  allowing it to maintain liquid states during charge/discharge cycles.<sup>[32]</sup> This may further enhance the cycle performance of LSBs by accommodating the large volume change of S without fracturing the electrode composite and maintaining the electrical conduction path.

In this work, we propose a mixture of sulfur, rGO, and Ga-based liquid metal (LM) as an LSB electrode composite to integrate the ability of rGO to trap the lithium polysulfide and the function of LM gallium as an electrocatalyst. Here, In and Sn were added to Ga to synthesize a LM with low melting point that maintains its liquid state at the LSB operating temperature, which plays a central role in this study. The LM allows the electrode composite to accommodate large volume change of sulfur in the charge/discharge process and prevents the fracture of the electrode that leads to the loss of the active material.

## Experimental

### Synthesis of reduced graphene oxide (rGO)

First, graphene oxide (GO) was synthesized by modified Hummers' method.<sup>[33,34]</sup> Two grams of graphite flakes (Alfa Aesar) were mixed with 50 mL of concentrated  $\text{H}_2\text{SO}_4$  in an ice bath. Eight grams of  $\text{KmnO}_4$  were then slowly added to the mixture. The temperature of the mixture was kept below  $10^\circ\text{C}$ . Then, the mixture was stirred in an ice bath below  $5^\circ\text{C}$  for 1 h. The oxidation reaction was sped up by heating the mixture to  $35^\circ\text{C}$  for 30 min. The exfoliation of oxidized graphite was carried out by adding of 500 mL of deionized water to the system followed by  $60^\circ\text{C}$  heating for 30 min.<sup>[35]</sup>  $\text{H}_2\text{O}_2$  was added to remove excess  $\text{KmnO}_4$ . The product was first washed by 2 M HCl and then three times by deionized water. The graphene oxide was obtained by lyophilization at 0.040 mbar and  $-40^\circ\text{C}$  using a Labconco freeze drying chamber. Reduced graphene oxide (rGO) was then obtained by thermal reduction of GO. The GO was heated to  $1000^\circ\text{C}$  in a pure argon atmosphere for 2 h.<sup>[36,37]</sup> The argon flow was kept at 30 SCCM.

### Preparation of rGO/S/LM electrode composite

Sulfur composite with a LM and rGO was prepared by the following steps (Figure 1a). First, a gallium-based LM used in this work was synthesized by mixing 68.5% Ga, 21.5% In and 10% Sn in a petri dish. The mixture became a room-temperature LM alloy within 4 h (see Supporting Information Figure S1). Sulfur, rGO, and the LM were then added to ethanol and sonicated in an ice bath to obtain smaller particles for 2 min, with 10-min pauses in between each cycle to prevent the solution from reaching a high temperature, for a total of 10 cycles. Here, a surfactant (lithium dodecyl sulfate, Sigma Aldrich) was added in the solution to reduce the size of LM to form nanoparticles.<sup>[38]</sup> After evaporating the ethanol, polyvinylidene fluoride (PVDF) and N-methyl-2-pyrrolidone solvent (NMP) were added to the mixture and stirred overnight to form a homogeneous slurry. Finally, the resultant slurry was dispersed on a carbon cloth with a diameter of 14 mm and dried overnight. Additionally, for comparison, control cells without LM were

prepared by mixing sulfur, rGO and PVDF with NMP solvent and dispersed on a carbon cloth.

### Materials characterization

The surface morphologies and elemental distribution on the surface of the rGO/S/LM electrode were characterized by a scanning electron microscope (SEM, ZEISS ULTRA 55) and a transmission electron microscope (TEM, FEI Tecnai F30). The chemical bonding of the electrode surface was investigated using X-ray photoelectron spectroscopy (XPS). The cells were disassembled in an argon filled glovebox after cycling and washed five times with 1,2 dimethoxyethane to remove excess electrolyte and dried overnight for characterizations. The TEM sample was prepared by dispersing sulfur, reduced graphene oxide and liquid metal nanoparticles in an ethanol solution and drop casting it onto a copper grid.

### Electrochemical performance

To investigate the effect of liquid metal nanoparticles, cells with rGO/S/LM and rGO/S were tested. The CR2026 coin cells were assembled inside an argon filled glovebox with lithium metal as an anode, rGO/S/LM and rGO/S as cathodes, and polypropylene (Celgard 2400) as a separator. The specific capacity was calculated based on the active weight of sulfur. The ratio that was used of LM to S is 1:3 and the loading mass of the active material was between  $0.65\text{--}0.78 \text{ mg cm}^{-2}$ . The electrolyte was prepared using 1 M lithium bis (trifluoromethanesulfonyl) imide (LiTFSI) mixed with a 1:1 ratio of 1,2-dimethoxyethane (DME) and 1,3-dioxolane (DOL). This mixture was then mixed with 2% LiNO<sub>3</sub>. The electrochemical measurements of the battery cells were tested using a multi-channel battery tester (Neware, BTS4000). Cyclic voltammetry (CV) was conducted at a scan rate of  $0.1 \text{ mV s}^{-1}$ , with a voltage range of  $1.5\text{--}3 \text{ V}$ . The electrochemical impedance (EIS) was carried out using a CHI 760E electrochemical station with an amplitude of 5 mV in the frequency range of  $10^{-1}$  to  $10^6 \text{ Hz}$ .

### Polysulfide dissolution test

0.8 g of sulfur, 0.23 g of Li<sub>2</sub>S and 0.069 of LiNO<sub>3</sub> were mixed in 10 mL of DME. A 1 M LiTFSI was then added to create the 0.5 M Li<sub>2</sub>S<sub>6</sub> catholyte.<sup>[39]</sup> The electrolyte was then stirred at  $60^\circ\text{C}$  for one day under an argon atmosphere to make a homogenous solution. The rGO/LM/S and rGO/S electrode were immersed in the catholyte, and its color change was observed.

### Ab initio simulation

To evaluate the ability of liquid metal to absorb lithium polysulfides, ab initio simulations were performed to calculate the adsorption energy of the polysulfides on the LM surface. First, 32 Ga, 9 In, and 5 Sn atoms were randomly placed in a  $10 \text{ \AA} \times 10 \text{ \AA} \times 10 \text{ \AA}$  unit cell and the molecular dynamics (MD) simulation was performed for 5 ps at  $300^\circ\text{C}$ , followed the structural optimization by conjugate gradient method. Then, 15 Å of a vacuum layer was added to the relaxed structure to create a slab model. Then, MD was performed using the slab model for 5 ps at  $300^\circ\text{C}$  followed by the structural relaxation. Here, atoms in the bottom few layers (3 Å total thickness) were fixed for the simulations of the slab models. After the optimization of the surface model was complete, a lithium polysulfide  $\text{Li}_2\text{S}_x$  ( $x=1, 2, 4, 6, 8$ ) was placed on the surface followed by MD for 5 ps at  $100^\circ\text{C}$  and the structural optimization. Finally, the binding energy  $E_{\text{binding}}$  was obtained by,

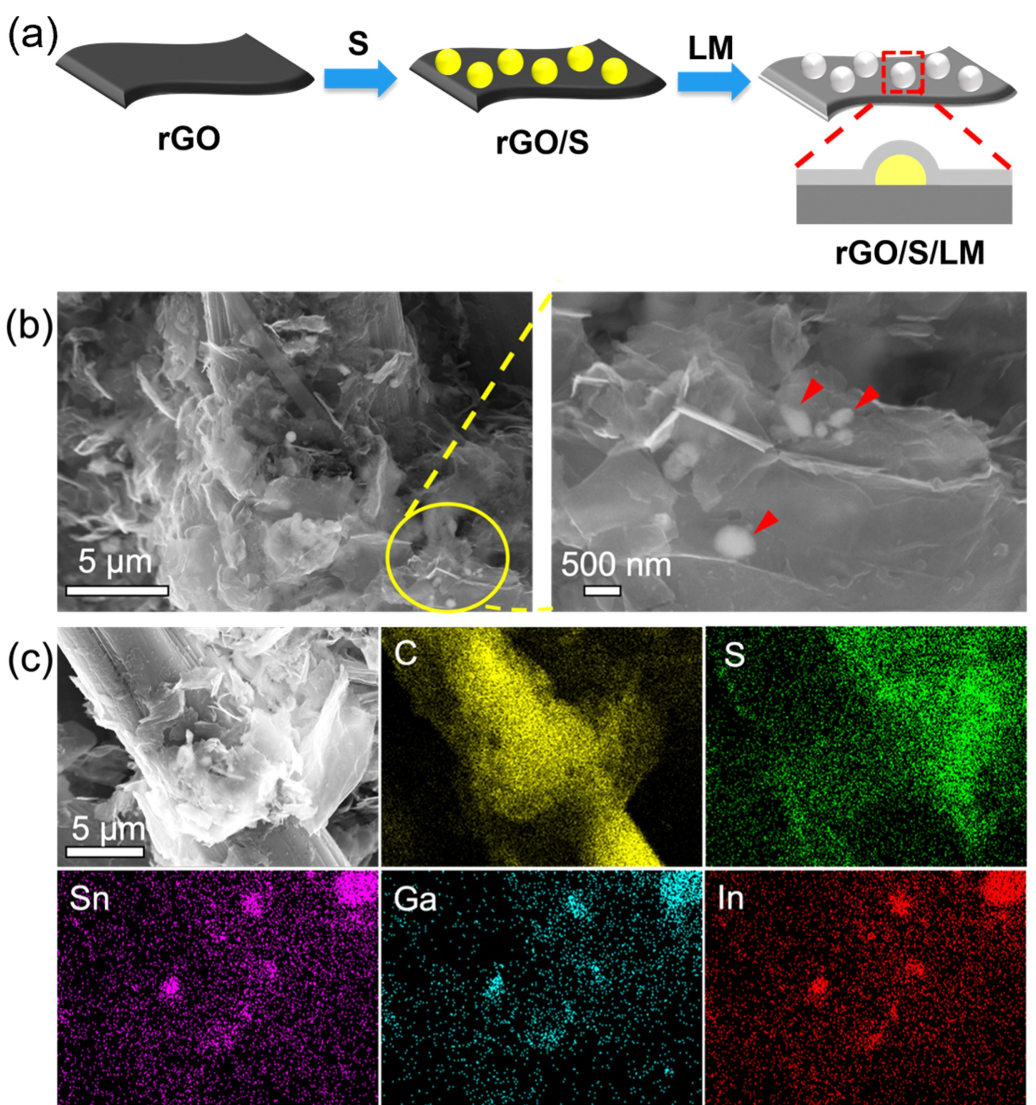


**Figure 1.** a) Schematic illustration of the preparation of rGO/S/LM cathode. b) SEM images and c) EDS elemental mapping of rGO/S/LM before cycling.

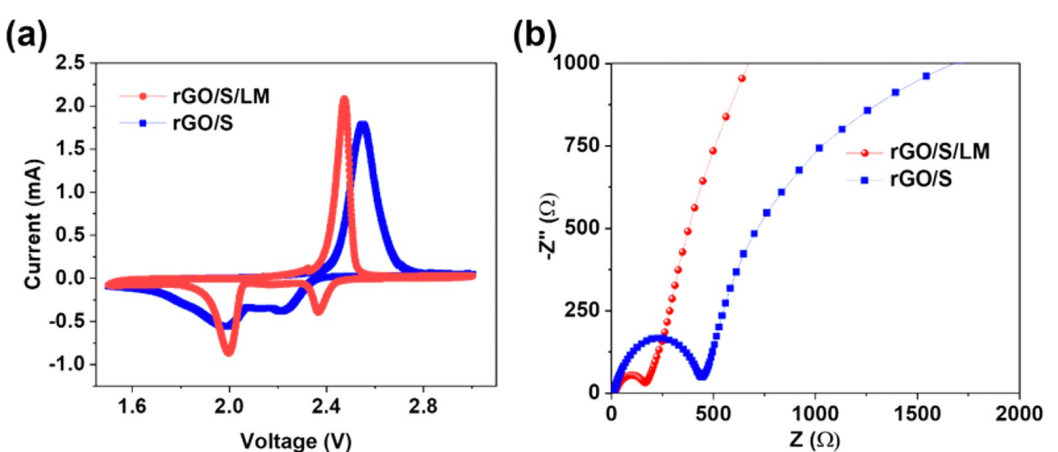


**Figure 2.** a) CV curves of rGO/S/LM and rGO/S cathodes. b) EIS spectra of rGO/S/LM and rGO/S cathodes.

$-E_{\text{binding}} = E_{\text{total}} - (E_{\text{LM}} + E_{\text{PS}})$ . Where,  $E_{\text{total}}$ ,  $E_{\text{LM}}$ , and  $E_{\text{PS}}$  are energies of the polysulfide on LM surface, the LM surface, and the

polysulfide molecule, respectively. Vienna Ab initio Simulation Package (VASP)<sup>[40,41]</sup> was employed in the simulation using the

same parameters described elsewhere.<sup>[24]</sup> The ionic cores were represented with a projected augment wave (PAW) potential.<sup>[42,43]</sup> A plane-wave energy cut-off of 500 eV and a generalized gradient approximation (GGA) parameterized by Perdew, Burke and Ernzerhof<sup>[44]</sup> were used for the exchange-correlation functional, and only  $\Gamma$ -point was selected for the k-mesh in the calculation.

## Results and Discussion

The SEM images and EDS elemental mapping of the rGO/S/LM electrode before cycling are shown in Figure 1(b and c). The LM dispersion was mostly uniform within the reduced graphene oxide and sulfur and deposited on the 3D conductive framework of the carbon cloth. However, some aggregated particles of LM were present. The small nano particles indicated by the arrow heads in the magnified SEM image (Figure 1b) are LM nano particles that did not spread on the rGO. STEM EDS and

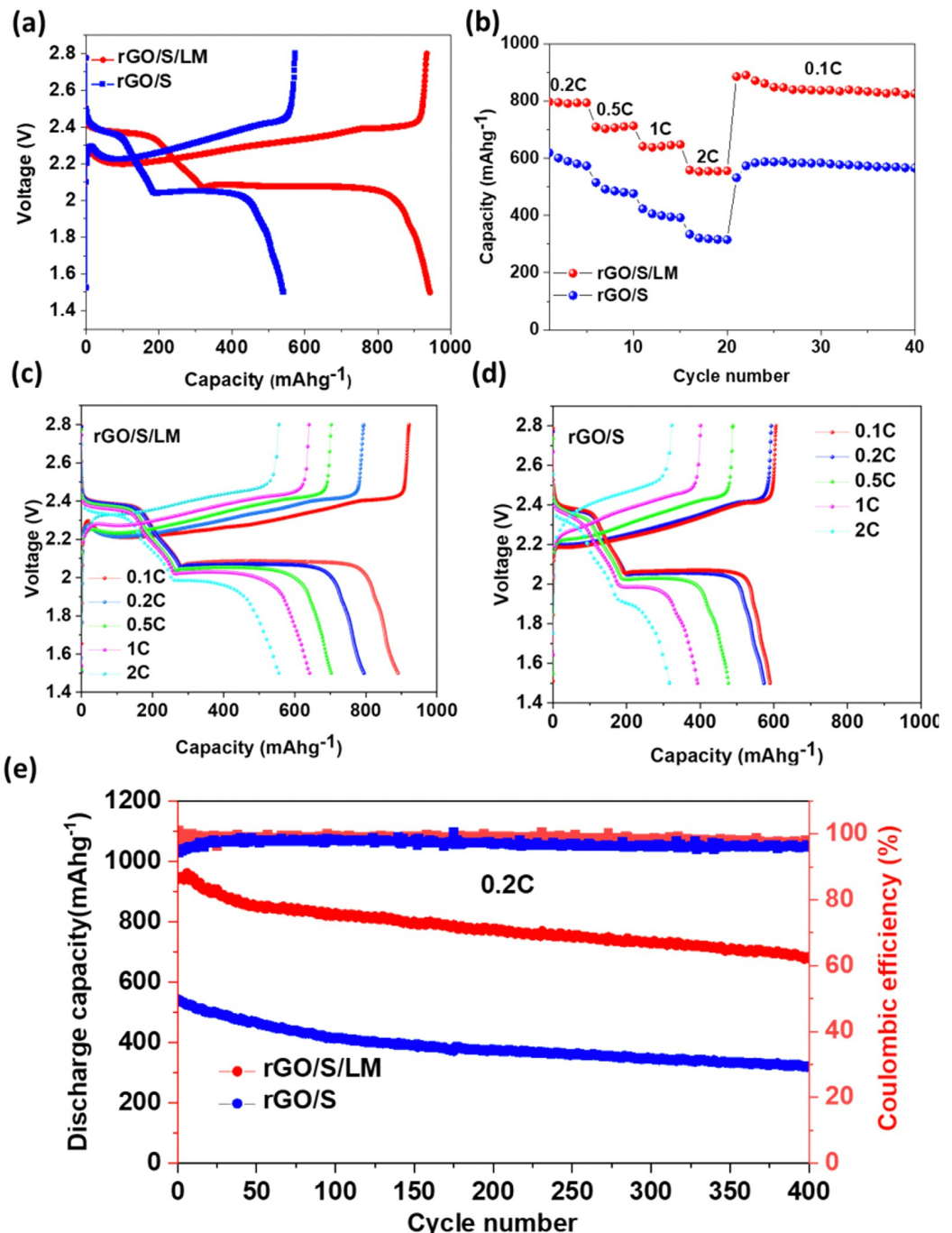


**Figure 3.** Electrochemical performances of rGO/S/LM and rGO/S cathodes: a) charge-discharge profile at 0.2 C, b) rate capabilities, c and d) charge-discharge profiles at different rates, e) cycling stability at 0.2 C for 400 cycles.

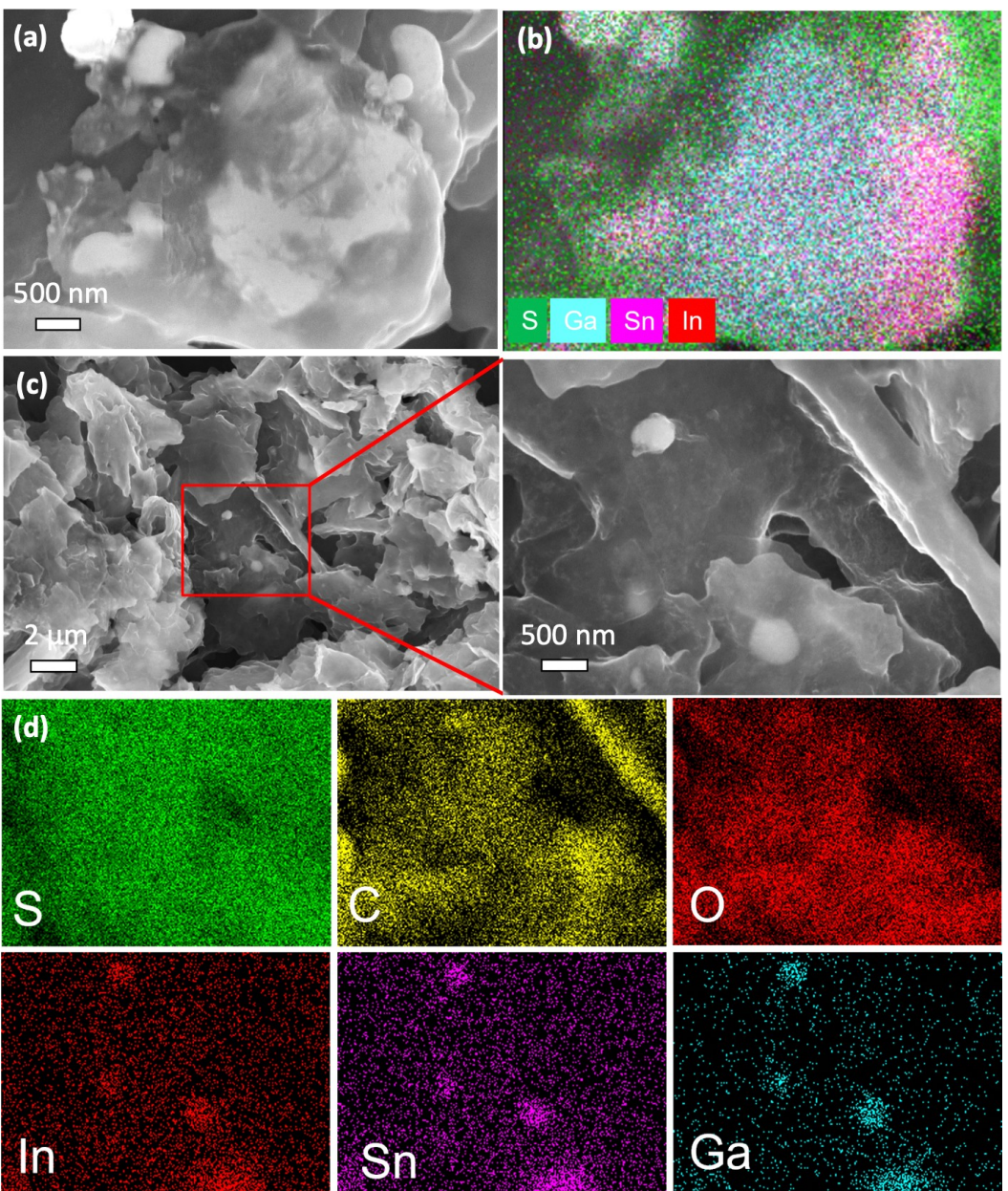


**Figure 4.** a) SEM image of rGO/S/LM after second discharge. b) EDS mapping of rGO/S/LM after second discharge. c) SEM images of rGO/S/LM after 100 cycles. d) Elemental mapping of rGO/S/LM corresponding to (c\_right image) after 100 cycles.

electron diffraction analysis of rGO/S/LM were also conducted to confirm that these particles were LM (consisting of Ga, Sn, and In) and the presence of LM on rGO (see Supporting Information for details). These observations confirm that LM was well mixed with sulfur and bound to rGO flakes although there were some agglomerated LM particles.

The cyclic voltammetry (CV) curves of rGO/S/LM and rGO/S cathodes are shown in Figure 2(a). Two cathodic peaks and one anodic peak of typical LSB reactions are clearly seen for both samples. The two cathodic peaks of rGO/S/LM, located at 2.36 V and ~2 V, correspond to the reduction of sulfur to polysulfides and to lithium sulfides  $\text{Li}_2\text{S}_2/\text{Li}_2\text{S}$ , the one sharp anodic peak located at 2.5 V represents the oxidation of  $\text{Li}_2\text{S}_2/\text{Li}_2\text{S}$  to

polysulfides and to sulfur. Compared to the rGO/S cathode, the rGO/S/LM exhibits higher intensity cathodic peaks at higher voltages and sharper anodic peak at lower potential, which demonstrates the lower over potential and enhanced reaction kinetics of the rGO/S/LM cathode. Electrochemical impedance spectroscopy (EIS) measurements were conducted for the rGO/S/LM and rGO/S cathodes to further analyze the reaction kinetics. Both samples showed one semicircle in the high to low frequency region, representing charge transfer resistance ( $R_{ct}$ ) and one sloping line in the low frequency region (Warburg impedance) as shown in Figure 2(b). In addition, the rGO/S/LM cathode has a smaller semicircle compared to the rGO/S,

demonstrating better charge transfer resistance and enhanced reaction kinetics.

Galvanostatic charge-discharge tests were conducted to evaluate the electrochemical performance of the rGO/S/LM and rGO/S cathodes. The charge-discharge profiles of rGO/S/LM and rGO/S at 0.2 C (Figure 3a) show two discharge plateaus

(corresponding to the formation of the high and low order lithium polysulfides) and one charge plateau. Both plateaus agreed with CV curves. Comparatively, rGO/S/LM shows a longer discharge profile and higher initial discharge capacity. Additionally, the voltage hysteresis between the charge and discharge plateaus for rGO/S/LM was smaller compared to that

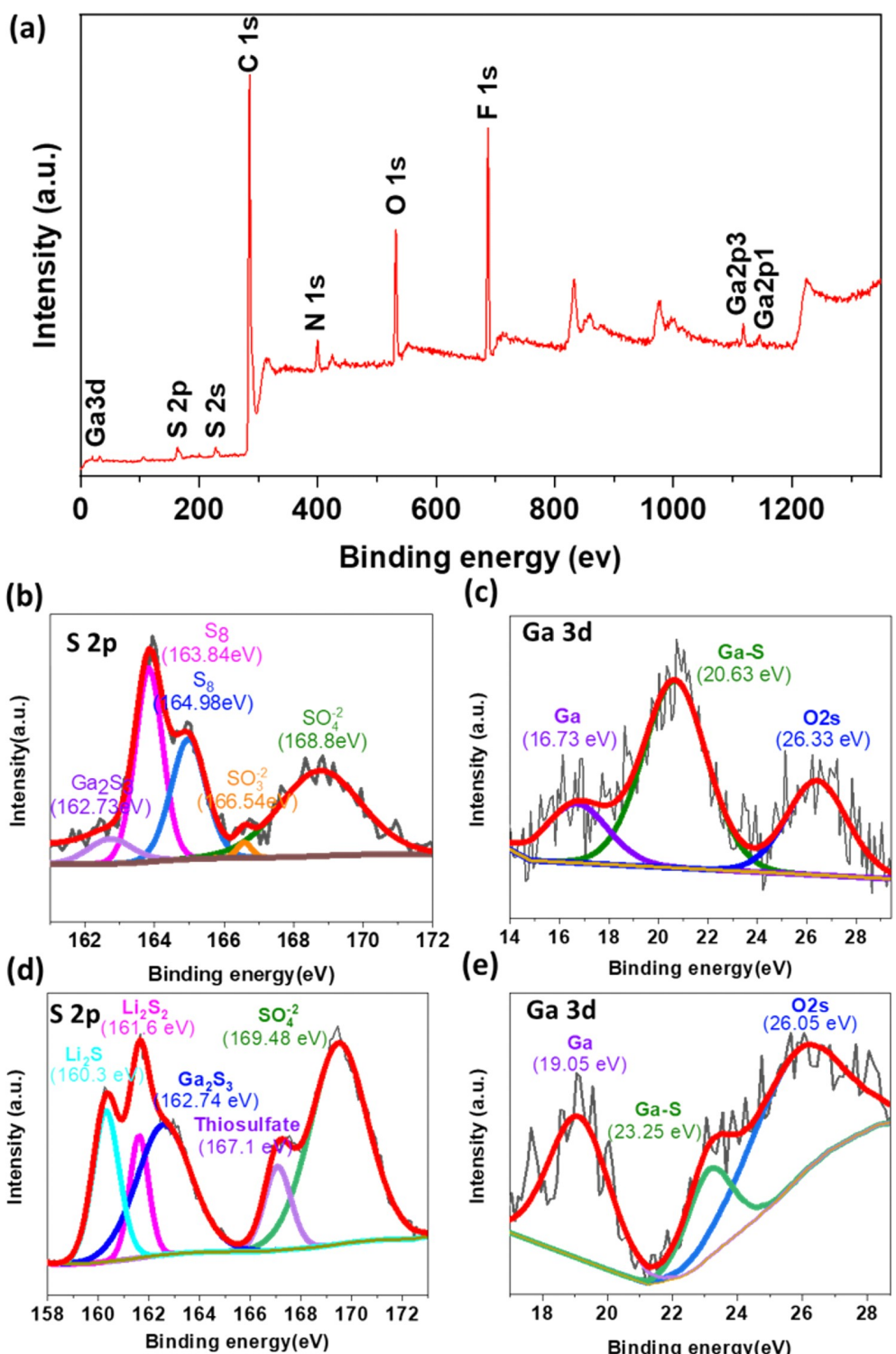


**Figure 5.** a) XPS spectrum of rGO/S/LM cathode before cycling. b and c) XPS spectra of sulfur and gallium before cycling. d and e) XPS spectra of sulfur and gallium after 100 cycles (discharge process).

of rGO/S. The lower polarization of the rGO/S/LM indicates a good reversibility and faster redox reaction kinetics owing to the catalytic effect of LM nanoparticles that accelerate polysulfide conversion reaction.

The rate performances of rGO/S/LM and rGO/S at different current densities are shown in Figure 3(b). The rGO/S/LM displays higher discharge capacities at 0.1, 0.2, 0.5, 1 and 2 C compared to rGO/S, and the capacity was successfully recovered when switched back to 0.1 C, revealing the good reversibility of rGO/S/LM cathode and the good capability of LM nanoparticles to trap lithium polysulfide. The voltage charge discharge profiles at various current rates (0.1–2 C) of rGO/S/LM and rGO/S are shown in Figure 3(c and d). As displayed in Figure 3(c), the two discharge plateaus of the rGO/S/LM are still obvious even at a higher current density (2 C).

Figure 3(e) shows the cycling performance of rGO/S/LM and rGO/S electrodes at 0.2 C (after five cycles of activation<sup>[45]</sup> at 0.1 C), with the rGO/S/LM cell exhibiting high discharge capacity (943.2 mAhg<sup>-1</sup>) and good Coulombic efficiency (over 96%) while rGO/S showed much lower capacity (540 mAhg<sup>-1</sup>). Moreover, the rGO/S/LM cell still maintained a good capacity retention (72.15%) even after 400 cycles, whereas the capacity retention of the rGO/S was only 59%. These results demonstrate the effectiveness of liquid metal nanoparticles to hinder the polysulfide shuttle effect and to enhance the cycling stability of the lithium sulfur battery.

In addition, SEM and energy dispersive X-ray spectroscopy (EDS) analyses were conducted to investigate the morphology and elemental distribution on the surface of the electrode after second and 100 cycles. The SEM images after second (Figure 4a) and 100 cycles (Figure 4c and d) indicate no obvious changes or cracks in the structure of the electrode. Moreover, EDS mappings after second and 100 cycles (Figure 4b and e) confirm that sulfur, carbon, tin, gallium, and indium were present and uniformly distributed on the surface of the electrode after the charge/discharge cycles. These results further confirm the liquid characteristic of LM to freely alter its shape contributes to accommodating the volume changes during cycling to prevent the detachment of sulfur from the current collector.

Furthermore, X-ray photoelectron spectroscopy (XPS) was conducted to investigate the element composition of the electrode before cycling and after 100 cycles. The XPS spectrum survey before cycling (Figure 5a) revealed that gallium, sulfur, carbon, nitrogen, oxygen, and fluoride are present on the surface of the electrode. In Figure 5(b), the high-resolution spectrum of S 2p before cycling reveals that the peak located at 162.73 eV is composed of Ga<sub>2</sub>S<sub>3</sub><sup>[29,46]</sup> in addition to the peaks from S<sub>8</sub>. This indicates that sulfur is chemically bound to LM nanoparticles. The peaks located at 166.54 and 168.8 eV are attributed to SO<sub>3</sub><sup>2-</sup> and SO<sub>4</sub><sup>2-</sup>, respectively. After 100 cycles (Figure 5d), the peaks at 160.3 and 161.6 eV<sup>[47-49]</sup> confirm that sulfur, after discharge, transforms to Li<sub>2</sub>S and Li<sub>2</sub>S<sub>2</sub>, respectively. The thiosulfate peak,<sup>[47,50,51]</sup> located at 167.2 eV is formed by the redox reaction between lithium polysulfides and gallium oxide, indicating the catalytic effect of the LM nanoparticle and its strong binding to lithium polysulfide. The high-resolution

spectrums of Ga 5d before and after discharge are shown in Figure 5c and e, respectively. The intensity of the GaS peak is higher than that of the Ga peak before cycling which validates the reaction of gallium with sulfur on the surface.<sup>[29,30]</sup> These results confirm the strong binding of sulfur particles which promote redox reaction kinetics by enhancing the transformation of lithium polysulfide to lithium sulfide.

To evaluate the catalytic effect of LM towards lithium polysulfide conversion, CV tests were performed using symmetric cells<sup>[52,53]</sup> in a voltage range of -1.0 to 1.0 V. Two symmetric cells were assembled using rGO/LM and rGO electrodes. A Celgard separator with 50 µL of 0.5 M Li<sub>2</sub>S<sub>6</sub> electrolyte was used for both cells (the results are shown in Supplementary Information Figure S4). The rGO/LM electrode exhibited higher redox current density compared to the rGO electrode, revealing the improved redox kinetics of the polysulfide conversion by the catalytic effect of LM.

To further confirm the ability of LM to prevent polysulfide dissolution, rGO/S/LM and rGO/S electrodes were immersed in 4 mL and 2 mL of 5 mM Li<sub>2</sub>S<sub>6</sub> DOL/DME and left for few hours to discern the color change of the solutions. The color of the solution with rGO/S electrode became darker after immersion in the solution while the one with rGO/S/LM electrode revealed no color change (Supporting Information Figure S5). This result indicates the addition of LM inhibited polysulfide dissolution due to its strong binding with S.

The ability of LM to trap polysulfides was also evident from the *ab initio* simulation. Figure 6(a) shows the binding energy of the lithium polysulfides on the LM surface in comparison

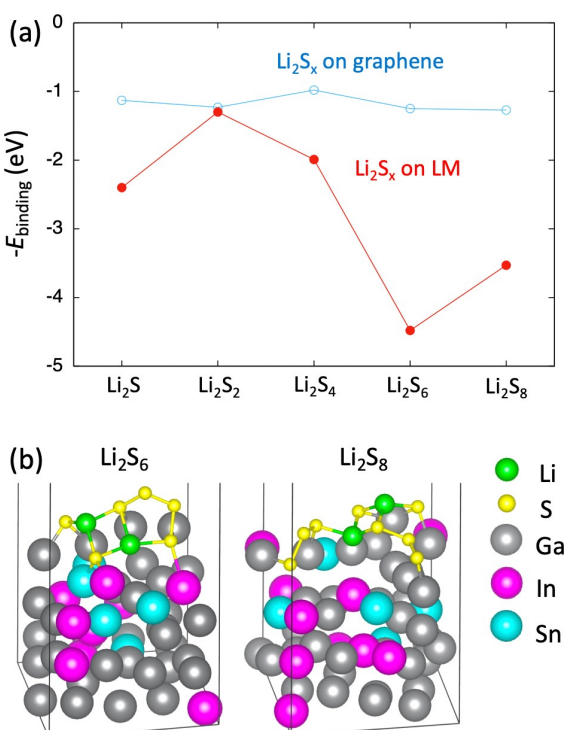


Figure 6. a) Calculated binding energies of lithium polysulfides on the LM surface, in comparison with graphene (data from Ref. [24]). b) Atomic structures of Li<sub>2</sub>S<sub>6</sub> and Li<sub>2</sub>S<sub>8</sub> adsorbed on the LM surface.

with those on graphene.<sup>[24]</sup> The binding energies of the polysulfides on graphene are low and almost constant regardless of the polysulfide species. In contrast, the binding energies are much higher on the LM surface particularly for the long-chained lithium polysulfides ( $\text{Li}_2\text{S}_6$  and  $\text{Li}_2\text{S}_8$ ). This can be attributed to the strong binding of S on LM (especially with Ga atoms) as seen in the molecular adsorption structures in Figure 6(b). It is worth noting that  $\text{Li}_2\text{S}_8$  ring was opened and spread on the LM surface leading to the formation of more atomic bonds between them. These results agree well with the XPS analysis showing Ga–S peak. The outcome of the simulation supports the improved polysulfide trapping by adding LM in the electrodes for high S-containing species. On the other hand, binding energy of  $\text{Li}_2\text{S}_n$  on  $\text{TiO}_2$  increases with decreasing  $n$  favoring adsorption of low S-containing species.<sup>[24]</sup> This suggests the possibilities of combining different polysulfide-trapping agents optimized to capture the entire series of the polysulfides.

## Conclusion

In conclusion, an LSB electrode composite consisting of LM, sulfur, and rGO (rGO/S/LM) was developed and demonstrated enhancement of the electrochemical performance of LSB battery. The added rGO and LM effectively trap polysulfide and prevent the shuttle effect, prolonging the cycle lifetime of the battery. LM also contributes to the faster redox reaction kinetics and accommodates large volume changes of the sulfur during the battery cycles. These characteristics of LM enhanced sulfur utilization, reduced reaction overpotentials, and prevented the loss of sulfur due to the electrode fracture, resulting in the improved capacity and cycle lifetime. The cell with rGO/S/LM cathode exhibited a higher discharge capacity of  $943.2 \text{ mAh g}^{-1}$  at 0.2 C, better coulombic efficiency, and greater rate performance at 2 C, compared with the control electrode without LM. rGO/S/LM maintained a good cycling stability even after 400 cycles. In addition, SEM analysis of the rGO/S/LM electrode after cycling showed no change in the structure from the initial state. The improved catalytic activity for the redox kinetics of the polysulfides was verified by the CV of the symmetric cell using rGO/LM and rGO, and the ability of LM to trap the polysulfides were confirmed by the dissolution experiment and the *ab initio* simulation. The dual function of the Ga-based LM to improve the electrochemical performance and mechanical stability is anticipated to open a new path towards practical lithium sulfur batteries. The application of LM is highly effective in overcoming two of the major challenges in LSBs: polysulfide dissolution and large volume changes of sulfur during LSB operations.

## Acknowledgements

The authors acknowledge Prof. Yang Yang in NSTC at UCF for equipment support on EIS measurement. SF thanks Higher Committee for Education Development in Iraq scholarship.

## Conflict of Interest

The authors declare no conflict of interest.

## Data Availability Statement

Research data are not shared.

**Keywords:** catalytic effect · liquid metal · lithium polysulfide trapping · lithium-sulfur battery · shuttle effect

- [1] M. Armand, J.-M. Tarascon, *Nature* **2008**, *451*, 652–657.
- [2] N.-S. Choi, Z. Chen, S. A. Freunberger, X. Ji, Y.-K. Sun, K. Amine, G. Yushin, L. F. Nazar, J. Cho, P. G. Bruce, *Angew. Chem. Int. Ed.* **2012**, *51*, 9994–10024; *Angew. Chem.* **2012**, *124*, 10134–10166.
- [3] J. B. Goodenough, K.-S. Park, *J. Am. Chem. Soc.* **2013**, *135*, 1167–1176.
- [4] B. L. Ellis, K. T. Lee, L. F. Nazar, *Chem. Mater.* **2010**, *22*, 691–714.
- [5] L. Yang, Q. Li, Y. Wang, Y. Chen, X. Guo, Z. Wu, G. Chen, B. Zhong, W. Xiang, Y. Zhong, *Ionics* **2020**, *26*, 5299–5318.
- [6] D. A. Boyd, *Angew. Chem. Int. Ed.* **2016**, *55*, 15486–15502; *Angew. Chem.* **2016**, *128*, 15712–15729.
- [7] B. Meyer, *Chem. Rev.* **1976**, *76*, 367–388.
- [8] Y. Mikhaylik, J. Akridge, *J. Electrochem. Soc.* **2004**, *151*, A1969–A1976.
- [9] S. Waluś, G. Offer, I. Hunt, Y. Patel, T. Stockley, J. Williams, R. Purkayastha, *Energy Storage Mater.* **2018**, *10*, 233–245.
- [10] J. He, A. Manthiram, *Energy Storage Mater.* **2019**, *20*, 55–70.
- [11] S. Li, B. Jin, X. Zhai, H. Li, Q. Jiang, *ChemistrySelect* **2018**, *3*, 2245–2260.
- [12] W. Y. Lee, E. M. Jin, J. S. Cho, D.-W. Kang, B. Jin, S. M. Jeong, *Energy* **2020**, *212*, 118779.
- [13] J. Schuster, G. He, B. Mandlmeier, T. Yim, K. T. Lee, T. Bein, L. F. Nazar, *Angew. Chem. Int. Ed.* **2012**, *51*, 3591–3595; *Angew. Chem.* **2012**, *124*, 3651–3655.
- [14] Z. Ma, L. Tao, D. Liu, Z. Li, Y. Zhang, Z. Liu, H. Liu, R. Chen, J. Huo, S. Wang, *J. Mater. Chem. A* **2017**, *5*, 9412–9417.
- [15] C. Zhang, H. B. Wu, C. Yuan, Z. Guo, X. W. (David) Lou, *Angew. Chem. Int. Ed.* **2012**, *51*, 9592–9595; *Angew. Chem.* **2012**, *124*, 9730–9733.
- [16] G. Zheng, Q. Zhang, J. J. Cha, Y. Yang, W. Li, Z. W. Seh, Y. Cui, *Nano Lett.* **2013**, *13*, 1265–1270.
- [17] G. Zhou, H. Tian, Y. Jin, X. Tao, B. Liu, R. Zhang, Z. W. Seh, D. Zhuo, Y. Liu, J. Sun, J. Zhao, C. Zu, D. S. Wu, Q. Zhang, Y. Cui, *Proc. Nat. Acad. Sci.* **2017**, *114*, 840–845.
- [18] X. Tao, J. Wang, Z. Ying, Q. Cai, G. Zheng, Y. Gan, H. Huang, Y. Xia, C. Liang, W. Zhang, Y. Cui, *Nano Lett.* **2014**, *14*, 5288–5294.
- [19] M. Yu, J. Ma, H. Song, A. Wang, F. Tian, Y. Wang, H. Qiu, R. Wang, *Energy Environ. Sci.* **2016**, *9*, 1495–1503.
- [20] X. Judez, H. Zhang, C. Li, J. A. González-Marcos, Z. Zhou, M. Armand, L. M. Rodríguez-Martínez, *J. Phys. Chem. Lett.* **2017**, *8*, 1956–1960.
- [21] J. Pan, G. Xu, B. Ding, Z. Chang, A. Wang, H. Dou, X. Zhang, *RSC Adv.* **2016**, *6*, 40650–40655.
- [22] S. Fahad, Z. Wei, A. Kushima, *J. Power Sources* **2021**, *506*, 230175.
- [23] Y.-S. Su, A. Manthiram, *Chem. Commun.* **2012**, *48*, 8817.
- [24] G. Xu, Q. Yan, S. Wang, A. Kushima, P. Bai, K. Liu, X. Zhang, Z. Tang, J. Li, *Chem. Sci.* **2017**, *8*, 6619–6625.
- [25] S.-H. Chung, A. Manthiram, *J. Phys. Chem. Lett.* **2014**, *5*, 1978–1983.
- [26] F. Liu, J. Liang, C. Zhang, L. Yu, J. Zhao, C. Liu, Q. Lan, S. Chen, Y.-C. Cao, G. Zheng, *Results Phys.* **2017**, *7*, 250–255.
- [27] S. Luo, M. Yao, S. Lei, P. Yan, X. Wei, X. Wang, L. Liu, Z. Niu, *Nanoscale* **2017**, *9*, 4646–4651.
- [28] M. Zhu, S. Li, B. Li, S. Yang, *Nanoscale* **2019**, *11*, 412–417.
- [29] S. Li, W. Zhang, J. Liu, Y. Zhang, Y. Zheng, *Appl. Surf. Sci.* **2021**, *563*, 150381.
- [30] S. Li, X. Zhang, H. Chen, H. Hu, J. Liu, Y. Zhang, Y. Pan, Y. Zheng, *Electrochim. Acta* **2020**, *364*, 137259.
- [31] S. Kim, D. H. Kim, M. Cho, W. B. Lee, Y. Lee, *Chem. Eng. J.* **2021**, *420*, 129772.
- [32] P. Surmann, H. Zeyat, *Anal. Bioanal. Chem.* **2005**, *383*, 1009–1013.
- [33] W. S. Hummers, R. E. Offeman, *J. Am. Chem. Soc.* **1958**, *80*, 1339–1339.
- [34] G. I. Titelman, V. Gelman, S. Bron, R. L. Khalfin, Y. Cohen, H. Bianco-Peled, *Carbon* **2005**, *43*, 641–649.

- [35] J. Chen, Y. Zhang, M. Zhang, B. Yao, Y. Li, L. Huang, C. Li, G. Shi, *Chem. Sci.* **2016**, *7*, 1874–1881.
- [36] Y. Zhu, M. D. Stoller, W. Cai, A. Velamakanni, R. D. Piner, D. Chen, R. S. Ruoff, *ACS Nano* **2010**, *4*, 1227–1233.
- [37] X. Gao, J. Jang, S. Nagase, *J. Phys. Chem. C* **2010**, *114*, 832–842.
- [38] Y. Lin, Y. Liu, J. Genzer, M. D. Dickey, *Chem. Sci.* **2017**, *8*, 3832–3837.
- [39] Y. Wu, X. Zhu, P. Li, T. Zhang, M. Li, J. Deng, Y. Huang, P. Ding, S. Wang, R. Zhang, J. Lu, G. Lu, Y. Li, Y. Li, *Nano Energy* **2019**, *59*, 636–643.
- [40] G. Kresse, J. Hafner, *Phys. Rev. B* **1993**, *47*, 558.
- [41] G. Kresse, J. Furthmüller, *Phys. Rev. B* **1996**, *54*, 11169.
- [42] P. E. Blöchl, *Phys. Rev. B* **1994**, *50*, 17953.
- [43] G. Kresse, D. Joubert, *Phys. Rev. B* **1999**, *59*, 1758.
- [44] J. P. Perdew, K. Burke, M. Ernzerhof, *Phys. Rev. Lett.* **1996**, *77*, 3865.
- [45] A. Raghuandanandan, P. Periasamy, P. Ragupathy, *ACS Sustainable Chem. Eng.* **2019**, *7*, 276–284.
- [46] S. Li, X. Zhang, H. Chen, H. Hu, J. Liu, Y. Zhang, Y. Pan, Y. Zheng, *Electrochim. Acta* **2020**, *364*, 137259.
- [47] M. Wang, H. Yang, K. Shen, H. Xu, W. Wang, Z. Yang, L. Zhang, J. Chen, Y. Huang, M. Chen, D. Mitlin, X. Li, *Small Methods* **2020**, *4*, 2000353.
- [48] Y. Luo, N. Luo, W. Kong, H. Wu, K. Wang, S. Fan, W. Duan, J. Wang, *Small* **2018**, *14*, 1702853.
- [49] S. Niu, S.-W. Zhang, R. Shi, J. Wang, W. Wang, X. Chen, Z. Zhang, J. Miao, A. Amini, Y. Zhao, C. Cheng, *Energy Storage Mater.* **2020**, *33*, 73–81.
- [50] X. Liang, C. Hart, Q. Pang, A. Garsuch, T. Weiss, L. F. Nazar, *Nat. Commun.* **2015**, *6*, 5682.
- [51] S. Huang, Y. Wang, J. Hu, Y. V. Lim, D. Kong, Y. Zheng, M. Ding, M. E. Pam, H. Y. Yang, *ACS Nano* **2018**, *12*, 9504–9512.
- [52] S. Niu, S.-W. Zhang, R. Shi, J. Wang, W. Wang, X. Chen, Z. Zhang, J. Miao, A. Amini, Y. Zhao, C. Cheng, *Energy Storage Mater.* **2020**, *33*, 73–81.
- [53] Z. Du, X. Chen, W. Hu, C. Chuang, S. Xie, A. Hu, W. Yan, X. Kong, X. Wu, H. Ji, L.-J. Wan, *J. Am. Chem. Soc.* **2019**, *141*, 3977–3985.

Manuscript received: December 15, 2021

Revised manuscript received: February 14, 2022

Accepted manuscript online: March 4, 2022

Version of record online: March 23, 2022